

Three-Dimensional Computer-Aided Diagnosis Scheme for Detection of Colonic Polyps

Hiroyuki Yoshida*, *Member, IEEE*, and Janne Näppi

Abstract—We have developed a three-dimensional (3-D) computer-aided diagnosis scheme for automated detection of colonic polyps in computed tomography (CT) colonographic data sets, and assessed its performance based on colonoscopy as the gold standard. In this scheme, a thick region encompassing the entire colonic wall is extracted from an isotropic volume reconstructed from the CT images in CT colonography. Polyp candidates are detected by first computing of 3-D geometric features that characterize polyps, folds, and colonic walls at each voxel in the extracted colon, and then segmenting of connected components corresponding to suspicious regions by hysteresis thresholding based on these geometric features. We apply fuzzy clustering to these connected components to obtain the polyp candidates. False-positive (FP) detections are then reduced by computation of several 3-D volumetric features characterizing the internal structures of the polyp candidates, followed by the application of discriminant analysis to the feature space generated by these volumetric features. The locations of the polyps detected by our computerized method were compared to the gold standard of conventional colonoscopy. The performance was evaluated based on 43 clinical cases, including 12 polyps determined by colonoscopy. Our computerized scheme was shown to have the potential to detect polyps in CT colonography with a clinically acceptable high sensitivity and a low FP rate.

Index Terms—Colon cancer, computer-aided diagnosis, CT colonography, polyp detection, virtual colonoscopy.

I. INTRODUCTION

COLON cancer is the second leading cause of cancer deaths in the United States, with approximately 60 000 deaths/year [1]. Studies show that early detection and removal of colonic polyps can reduce the risk of colon cancer and, thus, result in a decrease in the mortality rate from colorectal cancer [2]. *Computed tomographic colonography* (CTC) or *virtual colonoscopy* is a technique for detecting colorectal neoplasms by using a computed tomography (CT) scan of the cleansed and air-distended colon [2]. Current CT technology allows a single image set of the colon to be acquired in 20–30 s, which translates into an easier, more comfortable examination than is available with other screening tests. Therefore, CTC has been advocated as a promising technique for providing mass screening for colorectal carcinoma [3]–[5].

For CTC to be a clinically practical means of screening for colon cancers, the technique must be feasible for interpreting

a large number of images in a time-effective fashion, and for detecting polyps and masses with high accuracy. Currently, however, the interpretation of an entire CTC examination is time-consuming [3], [6]. A typical CTC examination produces 150–350 axial CT images each for the supine and prone imaging data sets, yielding a total of 300–700 images/patient. Despite the recent advances in image-display techniques [7], studies show that the case interpretation time is still between 15 and 40 min even when reading is done by experts in abdominal imaging [3], [6]. The interpretation time for an entire CTC examination should be reduced substantially before CTC can be translated from the research area to routine clinical practice, and especially to the screening setting [8]. In addition, the diagnostic performance of CTC currently remains undetermined and prone to perceptual errors [3], [9]. Several studies have shown a high sensitivity of 80%–100% and a specificity of 80%–90% in the detection of polyps [10], [11], whereas others have reported a relatively low sensitivity of 40%–70% and a specificity of 70%–80% [12], [13]. It has been suggested that these differences in sensitivity and specificity for CTC are partly based on the undefined learning curve for the interpretation of CTC [14]. Moreover, the visibility and conspicuity of polyps and, thus, the accuracy of polyp detection, may depend on the image acquisition parameters and display methods, both of which are still under investigation [15], [16]. These factors increase the perceptual error even for experienced observers [9].

Computer-aided detection (CAD) of polyps is attractive because it has the potential to overcome the above difficulties with CTC [17]. A CAD scheme automatically detects polyps and masses in CTC images, and it provides the locations of suspicious polyps to radiologists. The “second opinion” offered by a CAD scheme has the potential to reduce radiologists’ interpretation time and to increase radiologists’ diagnostic performance in the detection of polyps. Reduction of interpretation time can be achieved if radiologists focus on the small number of regions indicated by the CAD scheme. Radiologists can quickly survey a large portion of the colon that is likely to be normal. An improvement in the detection performance can be achieved because CAD can potentially reduce radiologists’ perceptual errors.

In the past several years, investigators have developed prototype CAD schemes for detecting polyps with CTC. Summers *et al.* [18], [19] and Vining *et al.* [20], [21] have proposed CAD schemes that extract the surface of the colonic wall and evaluate the curvature of the surface to detect polyps. Paik *et al.* [22], [23] proposed a CAD scheme based on a contour normal method that is based on the directions of the normal vectors

Manuscript received June 12, 2001; revised October 29, 2001. This work was supported by grants from the University of Chicago Cancer Research Center and from the University of Chicago Cancer Research Center. *Asterisk indicates corresponding author.*

*H. Yoshida is with the Department of Radiology, The University of Chicago, Chicago, IL 60637 USA (e-mail: yoshida@uchicago.edu).

J. Näppi is with the Department of Radiology, The University of Chicago, Chicago, IL 60637 USA.

Publisher Item Identifier S 0278-0062(01)11215-2.

from air to tissue. These schemes showed a potential to detect polyps in CTC because they provided a high detection performance when they were applied to simulated polyps. However, these existing schemes suffered from either a low sensitivity or a high false-positive (FP) rate when they were applied to clinical cases. When these schemes are set to yield a clinically acceptable sensitivity of 85%–100%, the number of FPs increases in the range of 20 to more than 100/case [21], [23]. When the FP rate is set to a value of as low as 3.5, the sensitivity decreases to 50%–70% [19].

In this paper, we present a high-performance, fully automated 3-D CAD scheme based on our previously reported CAD scheme [17]. Similar to existing CAD schemes, our scheme extracts the colon in which the polyps are detected. However, our scheme is unique in that it extracts a thick region that encompasses the entire colonic wall (Section III). Other methods attempt to extract only the surface of the colon [18], [24]. Our approach has an advantage over the surface-generation method in that it can extract entire polyps, including their internal structure that can be used for the reduction of FPs. The surface-generation method has a risk of losing a part of the polyp, particularly the internal structure and, thus, may decrease the detection performance. This method of extracting colonic walls has been improved substantially over our previous method [17], so that we are able to extract a colonic wall alone and remove the small bowel and stomach adhering to the colonic wall based on a self-adjusting volume-growing technique (Section III-B).

We also use 3-D geometric features for the detection of polyps (Section IV). These geometric features are employed specifically for differentiating polyps from folds and from the colonic wall and, thus, they can be effective in maximizing sensitivity. In this paper, in particular, we develop a novel 3-D volumetric feature, directional gradient concentration, that characterizes the internal structures of polyps, folds, and stool, and we use this feature for reducing FPs (Section V). Unlike other schemes that tend to use features independently to remove FPs, we combine this and other, previously-reported volumetric features by a linear and a nonlinear classifier to reduce FPs substantially (Section VI). In this paper, in particular, we used a classifier based on quadratic discriminant analysis to achieve a high generality in the detection of polyps.

The remainder of this paper is organized as follows. Section II provides a brief overview of our 3-D CAD scheme. Section III presents an improved colon segmentation method. Section IV describes a method for the detection of polyp candidates based on geometric features. Section V introduces several volumetric features, which are combined by a classifier in Section VI to reduce FPs. Section VII presents methods for the evaluation of the performance of the CAD scheme. Sections VIII–X present the results, discussion, and conclusion.

II. OVERVIEW OF THE CAD SCHEME

A diagram of the detection scheme is shown in Fig. 1. First, for performing 3-D analysis of the colon and polyps, a 3-D volume, isotropic in the x , y , and z directions, is generated from the axial CT images in a CTC data set, by linear interpolation between the corresponding pixels on the adjacent slices. Then we

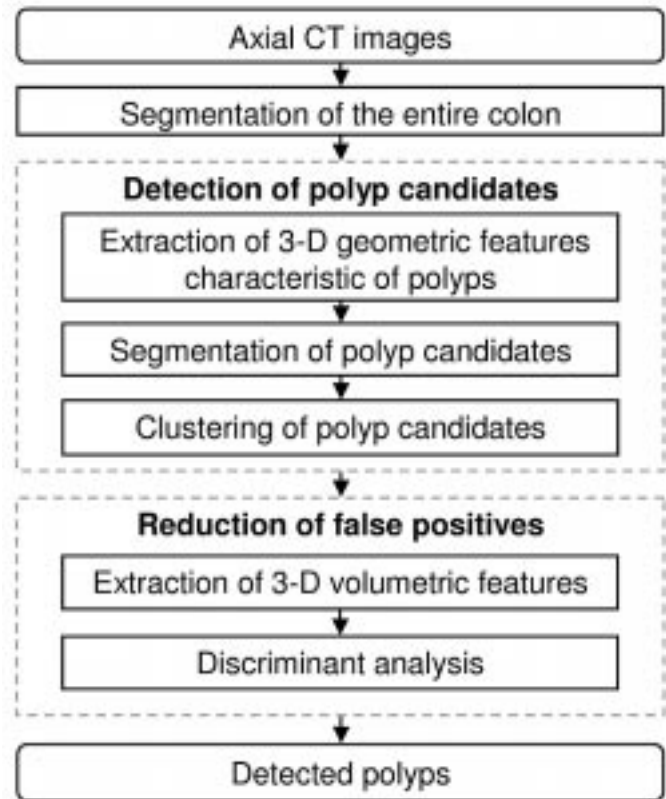


Fig. 1. Schematic diagram of the 3-D CAD scheme for the detection of polyps in CTC.

extract the colon by extracting a set of thick regions that encompass the entire colonic wall (Section III). Polyp candidates are detected (Section IV) first by computation of two 3-D geometric features characterizing polyps, folds, and colonic walls at each voxel of the segmented colon, and then segmentation of connected components by hysteresis thresholding using these geometric features. Fuzzy clustering is applied to these segmented components for obtaining the polyp candidates. FPs are then reduced by computation of 3-D volumetric features that characterize the internal structures of the polyp candidates (Section V). The final detected polyps are obtained by the application of discriminant analysis to the feature space generated by the volumetric features for these polyp candidates (Section VI).

The locations of the polyps detected by our computerized scheme are compared to those of conventional colonoscopy that is used as the gold standard. All of these processes are performed automatically, without human intervention.

III. KNOWLEDGE-GUIDED SEGMENTATION OF COLON

The isotropic volume generated by linear interpolation may contain large amounts of anatomic structures other than the colon. To limit the search space to the polyps within the colon, and to avoid generating FPs due to the extra-colonic structures, the entire colon is segmented by using a fully automated knowledge-guided technique. Specifically, we extract a set of thick regions that encompasses the entire colonic wall. Therefore, the extracted colonic wall contains not only the surface, but also the complete inner structure of the polyps.

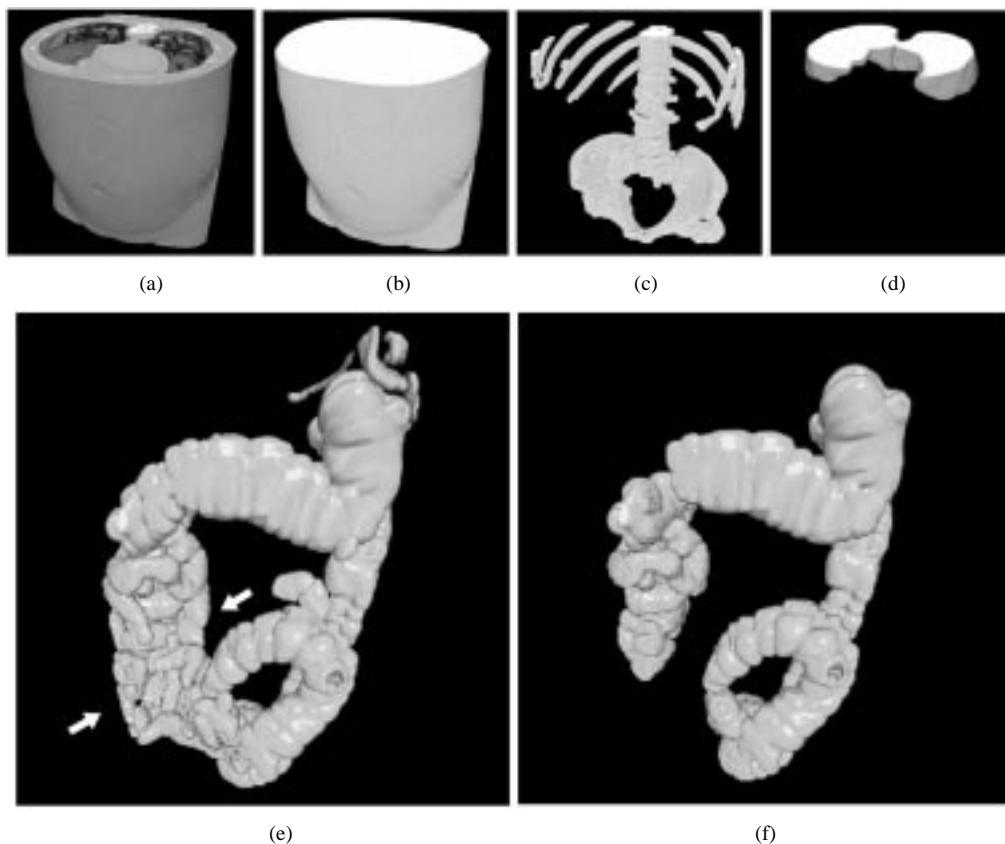


Fig. 2. Illustration of colon segmentation. (a) Original CT volume, and segmented (b) outer air (body shown), (c) bones, and (d) lung bases. (e) Segmented colon based on ABE. Parts of the small bowel (arrow) adhere to the colon. (f) Final segmented colon based on CBA. The parts of the small bowel adhering to the colon in (e) are removed, and a region encompassing the colon alone is extracted.

The process of colon segmentation consists of two major steps: 1) *anatomy-based extraction* (ABE) and 2) *colon-based analysis* (CBA) (Fig. 2). The ABE segments the colonic wall C with high sensitivity, but the resulting segmentation, denoted by \tilde{C}^+ , could contain redundant extra-colonic components, such as small bowel or stomach. Therefore, in the second step, the CBA produces a segmentation, denoted by \tilde{C}^- , that is used for removing the extra-colonic components from \tilde{C}^+ . The final segmentation \tilde{C} is a digital approximation of the actual colonic wall. Additional details of the technique are given elsewhere [25], [26].

In the following, the segmentation of a region A is denoted by \tilde{A} to distinguish between the actual region (e.g., colon) and its discrete segmentation. The complement of a subset (region) A in set B is denoted by $B \setminus A$. The union of two sets (regions) A and B is denoted by $A \cup B$, and the intersection is denoted by $A \cap B$.

A. Anatomy-Based Extraction

The ABE is similar to the anatomy-oriented colon segmentation scheme that we presented earlier [25]. The colon is segmented by application of the following methods to the 3-D isotropic volume: Gaussian smoothing, histogram analysis, thresholding, edge detection, region-growing, connected component analysis, and mathematical morphology.

Let V , R_a , R_b , and R_l denote the original CT volume, outer air (the region surrounding the body), bones, and lung

bases, respectively. Let $T_{CT}(\alpha, \beta)$ denote the operation of thresholding the CT value range $[\alpha, \beta]$. First, we search the global histogram of the original volume V for local maxima in predetermined ranges in order to find the characteristic peaks that correspond to CT values of air (L_A), fat (L_F), and muscle (L_M). Details of this procedure are described in [25]. Next, outer air, R_a , is segmented by $T_{CT}(-\infty, (L_A + L_F)/2)$, followed by a series of morphological operations and connected component analysis. The bone region R_b is segmented from $V \setminus \tilde{R}_a$ by $T_{CT}((2/3)L_M + 100, \infty)$. To segment lung bases R_l , we perform a local histogram analysis of the top region of $V \setminus (\tilde{R}_a \cup \tilde{R}_b)$. The lung bases are segmented by $T_{CT}((L_A + L_L)/2, L_L + 150)$, where L_L is the lung peak CT value of the local lung histogram (see [25]). The resulting connected components that are close to the estimated location of the left and right lung bases are removed.

The segmentation of R_a , R_b , and R_l is performed in reduced resolution to accelerate the colon segmentation process. To ensure that the boundary zone of these regions is also removed, the segmentations \tilde{R}_a , \tilde{R}_b and \tilde{R}_l are expanded by 2–8 mm by use of 3-D morphological dilation.

The colon is segmented from the remaining volume $V_c = V \setminus (\tilde{R}_a \cup \tilde{R}_b \cup \tilde{R}_l)$ by intersecting of the regions obtained by $T_{CT}(L_M - 800, L_M - 50)$ and $T_{GR}(L_M - 950, \infty)$, where T_{GR} denotes thresholding of the gradient magnitude. Let $\mathcal{P} = \{\mathcal{P}_i\}$ be the set of the resulting connected components, and let $|\mathcal{P}_i|$ denote the number of voxels in a component \mathcal{P}_i . The largest

component $\mathcal{P}_L \in \mathcal{P}$ represents the principal region of the colon. Additional components are included in the colon segmentation according to

$$\tilde{C}^+ = \mathcal{P}_L \cup \{\mathcal{P}_j; |\mathcal{P}_j| \geq 0.01|\mathcal{P}_L|, j \neq L, \mathcal{P}_j \in \mathcal{P}\}.$$

The set \tilde{C}^+ denotes the region segmented by ABE. The thickness of the segmented colonic wall is adjusted to 3–4 mm.

B. Colon-Based Analysis

The segmentation provided by the ABE is of the form

$$\tilde{C}^+ = (C \setminus c) \cup E',$$

where C represents the actual colonic walls $c \subset C$ is the portion of the colonic wall not segmented by the ABE, and E' represents extra-colonic components. For polyp detection, we may assume that $c = \emptyset$ (empty set), because, according to our observations, the portions of the colon not segmented by the ABE reside within completely collapsed regions that are not of diagnostic quality. On the other hand, up to 20% of the FP polyp findings of our original CAD scheme were found to originate from the extra-colonic components E' [17]. Therefore, to minimize E' , we developed the CBA technique, which essentially implements a self-adjusting volume-growing scheme to segment the air within the colonic lumen. Let \tilde{C}^- denote the segmentation produced by the CBA. The final segmentation of the colon is obtained by intersection of the two segmentations \tilde{C}^+ (ABE) and \tilde{C}^- (CBA)

$$\tilde{C} = \tilde{C}^+ \cap \tilde{C}^-. \quad (1)$$

The seed points of the volume-growing step in CBA are detected automatically from \tilde{C}^+ . The first seed is chosen from within the rectum, because this part of the colon can be located most reliably. First, a volume of interest V_R is extracted from the 4-cm bottom region of the CT volume that covers \tilde{C}^+ . Let $R_{\tilde{C}^+} = V_R \cap \tilde{C}^+$. Then $R_{\tilde{C}^+}^+$ divides $V_R \setminus R_{\tilde{C}^+}$ into two disconnected components: the colonic lumen and the region outside the colon. The rectum is identified as the second largest connected component within $V_R \setminus R_{\tilde{C}^+}$.

The method above assumes that the rectum is located in the bottom 4 cm of the CT volume that covers the ABE segmentation \tilde{C}^+ . If this is not the case, there are two options. First, the rectum can be located above this region. The only such cases we have encountered involve a collapsed rectum, where only a small isolated region of the rectum is segmented by the method. In this case, the volume-growing step continues as described below. In the second case, the rectum is located below the 4-cm region, and in this case the rectum is collapsed completely or is not contained within the original CT volume V . This situation may produce multiple disconnected fragments of colon, if these are connected in the region that is excluded from V . To detect such cases, we check the bottom 20% region of the CT volume covering \tilde{C}^+ after the CBA segmentation is completed, but before the final segmentation, \tilde{C} , is established. The connected components that do not extend above this 20% region are included in \tilde{C}^+ , if they cover a region of at least 1000 mm³, and are connected to the bottom CT slice of the region.

The volume-growing step may need to be continued if the complete colon is not segmented (the conditions are described below). Let r_i denote the region that has been segmented by the most recent volume-growing step. The updated CBA segmentation is the region $r'_i \cup \tilde{C}^-$, where r'_i represents r_i expanded to cover \tilde{C}^+ in the desired thickness within the local neighborhood of r_i . Then, if \tilde{C} obtained from (1) is still considered incomplete, the volume-growing process is continued by choice of a seed point from within the largest nonsegmented air-filled region.

Six conditions are used for testing whether \tilde{C} represents a complete colon. First, the amount of voxels removed from \tilde{C}^+ is limited according to $\tilde{C}_\Delta = (|\tilde{C}^+| - |\tilde{C}|) / |\tilde{C}^+| > 0.50$, where $|\tilde{C}|$ denotes the number of voxels within the segmented region. Second, the symmetry between the ascending and descending colon (C_a and C_d) is tested by checking whether the amount of segmented voxels between the expected locations of C_a and C_d differs by less than 20%. The third condition tests the presence of segmented colon within the expected location of the rectum. The fourth condition checks whether the colon represented by \tilde{C} passes within an offset of 10%–25% from the boundary of the CT volume that covers \tilde{C}^+ . The fifth condition tests whether there are very large air-filled components that have not been segmented. Finally, the sixth condition terminates the segmentation process if $\tilde{C}_\Delta > 0.95$.

IV. DETECTION OF POLYP CANDIDATES

Polyp candidates are detected in the segmented colon \tilde{C} by 1) computing of 3-D geometric features characterizing polyps, 2) segmenting of connected components corresponding to polyps, and 3) clustering of these connected components to generate polyp candidates.

A. Three-Dimensional Geometric Features Characterizing Polyps

For characterizing polyps, 3-D geometric features called the *volumetric shape index* and *curvedness* [27]–[29] are computed at each voxel in \tilde{C} . The volumetric shape index characterizes the topological shape of the volume in the vicinity of a voxel [see (8)], whereas the volumetric curvedness represents the size of the polyp or the magnitude of the effective curvature [see (9)]. Both quantities are defined based on the notion of curvature. Therefore, the definition and the computational method of curvature are described briefly in the following.

Curvature is a local property attached to points on a surface. Let $h(p)$ denote the CT value at a point (voxel) $p = (x, y, z)$. Then an iso-surface P at the level (CT value) of a in a 3-D space \mathbb{R}^3 is given by

$$P \equiv \{p = (x, y, z) \in \mathbb{R}^3; h(p) = a\}.$$

At each point p , there exists a small neighborhood U of p in which z can be expressed by a function ϕ of x and y . By denoting (x, y) with (u, v) in this neighborhood, one can represent the iso-surface P as

$$P(u, v) = \{(u, v) \in \mathbb{R}^2; h(u, v, \phi(u, v)) = a\}.$$

Let us denote the partial derivatives of P in terms of u and v as follows:

$$P_u \equiv \frac{\partial P(u, v)}{\partial u} \quad P_v \equiv \frac{\partial P(u, v)}{\partial v} \quad (2)$$

$$P_{uu} \equiv \frac{\partial^2 P(u, v)}{\partial^2 u} \quad P_{uv} \equiv \frac{\partial^2 P(u, v)}{\partial u \partial v}$$

$$P_{vv} \equiv \frac{\partial^2 P(u, v)}{\partial^2 v}. \quad (3)$$

With these notations, a vector parallel to the normal vector to the surface is defined as

$$Q \equiv \frac{P_u \times P_v}{\|P_u \times P_v\|}$$

where \times denotes the outer product of two vectors, and $\|\cdot\|$ denotes a norm. With these notations, the *first fundamental forms* [30] are defined as

$$E \equiv P_u \cdot P_u, \quad F \equiv P_u \cdot P_v, \quad G \equiv P_v \cdot P_v. \quad (4)$$

Also, the *second fundamental forms* [30] are defined as

$$L \equiv P_{uu} \cdot Q, \quad M \equiv P_{uv} \cdot Q, \quad N \equiv P_{vv} \cdot Q. \quad (5)$$

Because we are interested in calculating the curvature information at a voxel p without explicitly generating an iso-surface, we calculate the first and second fundamental forms directly from the isotropic volume as follows [31], [32]. By the use of implicit differentiation and the chain rule, we obtain $P_u = \partial P / \partial u = (1, 0, \partial \phi / \partial u) = (1, 0, -h_x / h_z)$. Substituting similar expressions for P_v , P_{uu} , P_{uv} , and P_{vv} into (3)–(5), we obtain

$$\begin{aligned} E &= 1 + \frac{h_x^2}{h_z^2} \\ F &= 1 + \frac{h_x h_y}{h_z^2} \\ G &= 1 + \frac{h_y^2}{h_z^2} \\ L &= \frac{(2h_x h_z h_{xz} - h_x^2 h_{zz} - h_z^2 h_{xx})}{R} \\ M &= \frac{(h_x h_z h_{yz} + h_y h_z h_{xz} - h_x h_y h_{zz} - h_z^2 h_{xy})}{R} \\ N &= \frac{(2h_y h_z h_{yz} - h_y^2 h_{zz} - h_z^2 h_{yy})}{R} \\ R &\equiv h_z^3 \sqrt{\frac{|h|}{h_z^2}} \quad |h| \equiv \sum_{i=x,y,z} h_i^2. \end{aligned} \quad (6)$$

Then the *principal curvatures* $\kappa_1(p)$ and $\kappa_2(p)$ [30], [33] are defined as

$$\begin{aligned} \kappa_1(p) &\equiv H(p) + \sqrt{H^2(p) - K(p)} \\ \kappa_2(p) &\equiv H(p) - \sqrt{H^2(p) - K(p)} \end{aligned} \quad (7)$$

where $K(p)$ and $H(p)$ are the *Gaussian curvature* and *mean curvature*, respectively, defined at p as follows:

$$\begin{aligned} K &\equiv \frac{LN - M^2}{EG - F^2} \\ &= \frac{1}{|h|^2} \sum_{(i,j,k)=\text{Perm}(x,y,z)} \{h_i^2 (h_{jj} h_{kk} - h_{jk}^2) \\ &\quad + 2h_j h_k (h_{ik} h_{ij} - h_{ii} h_{jk})\} \\ H &\equiv \frac{EN - 2FM + GL}{2(EG - F^2)} \\ &= \frac{1}{|h|^{3/2}} \sum_{(i,j,k)=\text{Perm}(x,y,z)} \{-h_i^2 (h_{jj} + h_{kk}) + 2h_j h_k h_{jk}\}. \end{aligned}$$

Here, $\text{Perm}(x, y, z)$ is a permutation of (x, y, z) , i.e., $\text{Perm}(x, y, z) \equiv \{(x, y, z), (y, z, x), (z, x, y)\}$.

By use of these principal curvatures, the volumetric shape index $SI(p)$ and the volumetric curvedness $CV(p)$ at a voxel p are defined as the local shape index and curvedness of the iso-surface that passes p [27]:

$$SI(p) \equiv \frac{1}{2} - \frac{1}{\pi} \arctan \frac{\kappa_1(p) + \kappa_2(p)}{\kappa_1(p) - \kappa_2(p)} \quad (8)$$

$$CV(p) \equiv \sqrt{\frac{\kappa_1(p)^2 + \kappa_2(p)^2}{2}} \quad (9)$$

where $\kappa_1 \neq \kappa_2$.

The space spanned by SI and CV is a polar-coordinate representation of the space spanned by the principal curvatures κ_1 and κ_2 . The shape index is a measure of the shape. Every distinct shape, except for the plane, corresponds to a unique value of SI [27], [28]. These shapes are mapped on a unit circle in the (κ_1, κ_2) -space (see, Fig. 3). The unit circle contains shapes with unit curvedness, and the rays through the origin contain identical shapes that differ in their curvedness, i.e., their sizes. For example, as shown in Fig. 3, five well-known shape classes have the following shape index values: cup (0.0), rut (0.25), saddle (0.5), ridge (0.75), and cap (1.0). Diagrammatically, opposite points on the unit circle, denoted by the end points of the dotted lines, represent shapes that are each other's "negative," that is, they have the same shape, but the opposite mold. Therefore, all shapes can be mapped on the interval $SI \in [0, 1]$. In Fig. 3, the "negative" shapes are represented by light gray. A plane has vanishing curvedness and an indeterminate shape index.

The most important advantage of the shape index in shape analysis is that the transition from one shape to another occurs continuously and, thus, the shape index can describe subtle shape variations effectively. For example, $SI = 0.875$ represents the "dome" shape, which is a transient shape from ridge ($SI = 0.75$) to cap ($SI = 1.0$). Moreover, the volumetric shape index introduced in this paper allows one to define the shape index at every voxel in a volume without explicitly calculating the iso-surface, because the definition of SI is based on the curvatures that are computed locally at the voxel as shown in (6) and (7). Therefore, the volumetric shape index captures the intuitive notion of local shape of an iso-surface at a voxel.

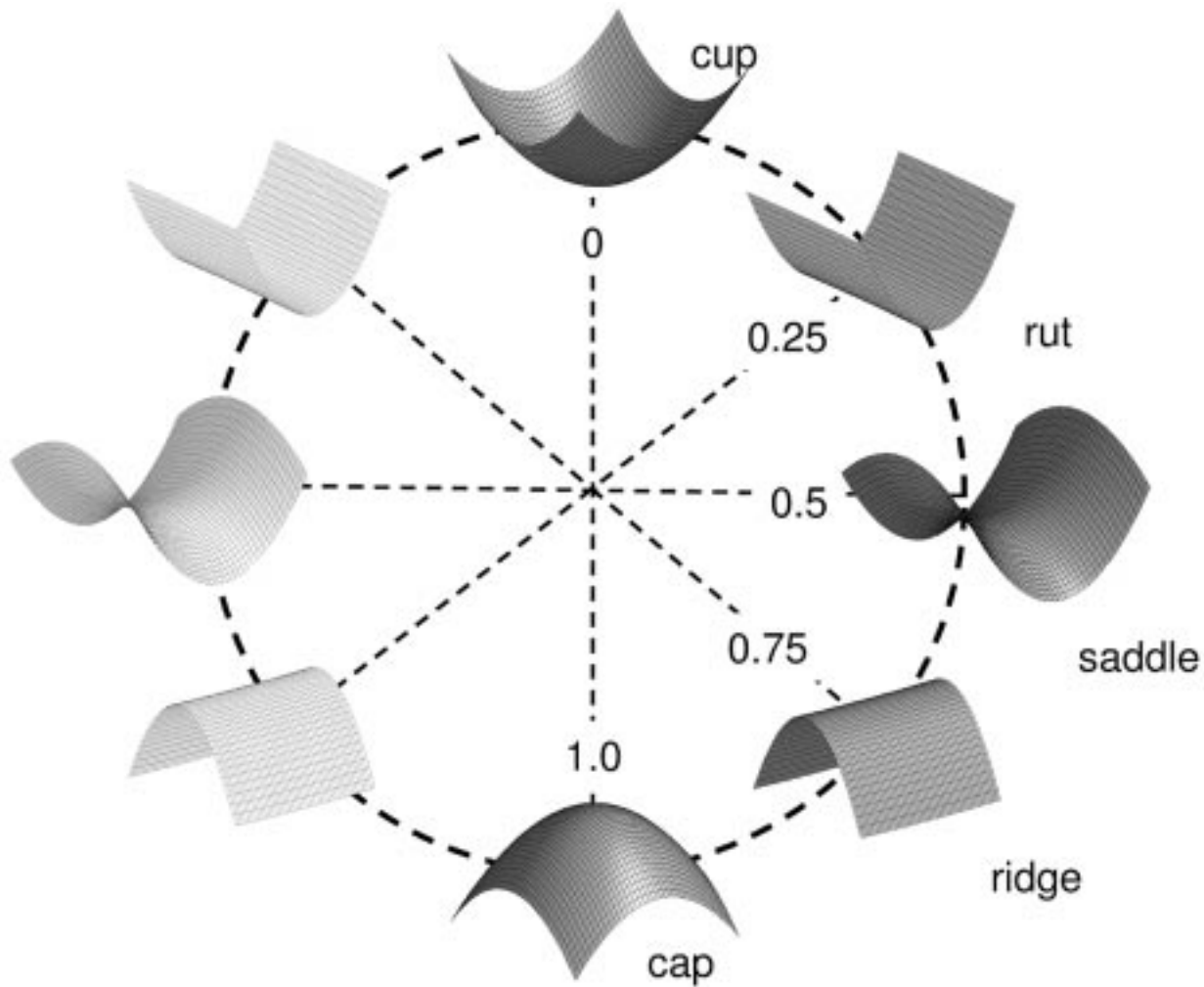


Fig. 3. Relationship of representative shapes to the shape index values.

The curvedness represents how gently curved the iso-surface is. The dimension of the curvedness is that of the reciprocal of length, and its range is $]-\infty, \infty[$. Curvedness is a “dual” feature to the shape index in that the shape index measures “which” shape the local neighborhood of a voxel has, whereas the curvedness measures “how much” shape the neighborhood includes. The curvedness also provides scale information: a large negative value implies a very gentle change, whereas a large positive value implies a very sharp knife-like edge.

In the 3-D volumetric data, generally, polyps appear as bulbous, cap-like structures adhering to the colonic wall, with small to medium curvedness, whereas folds appear as elongated, ridge-like structures with large curvedness values. The colonic walls appear as nearly flat, cup-like structures with small curvedness values. Therefore, the shape index and the curvedness can differentiate among polyps, folds, and colonic walls effectively.

Fig. 4 demonstrates the potential of the shape index in differentiating colonic structures. Fig. 4(a) and (d) shows axial CT images that contain a polyp in the region indicated by a box. Fig. 4(b) and (e) shows magnified views of the regions indicated in Fig. 4(a) and (d). The polyps are indicated by arrows. Fig. 4(c) and (f) represents 3-D endoscopic views of Fig. 4(b)

and (e), rendered by perspective volume rendering and by the shape index. Voxels that have shape index values corresponding to the cap class are rendered white, those corresponding to ridge are rendered light gray, and those corresponding to the other classes are rendered dark gray. As expected, most portions of the polyp are rendered white, whereas folds and colonic walls are rendered light gray and dark gray, respectively. With this rendering scheme, the polyps, folds, and colonic wall are clearly separated, and the polyps are easily distinguishable from other structures.

B. Segmentation of Polyp Candidates

The characteristic values of the shape index for polyps are used to segment the polyp candidates by use of *hysteresis thresholding* [34]. First, voxels that have shape index and curvedness values between a predefined minimum and maximum are extracted as *seed regions*. We set the minimum and maximum threshold values for the shape index to 0.9 and 1.0, respectively, so that we can select the regions that are in the cap class. The minimum and maximum threshold values for curvedness are set so that the curvedness is within the range of targeted polyps, i.e., minimum of 0.08 mm^{-1} (effective size of 12.5 mm) and maximum of 0.20 mm^{-1} (effective size of 5.0 mm).

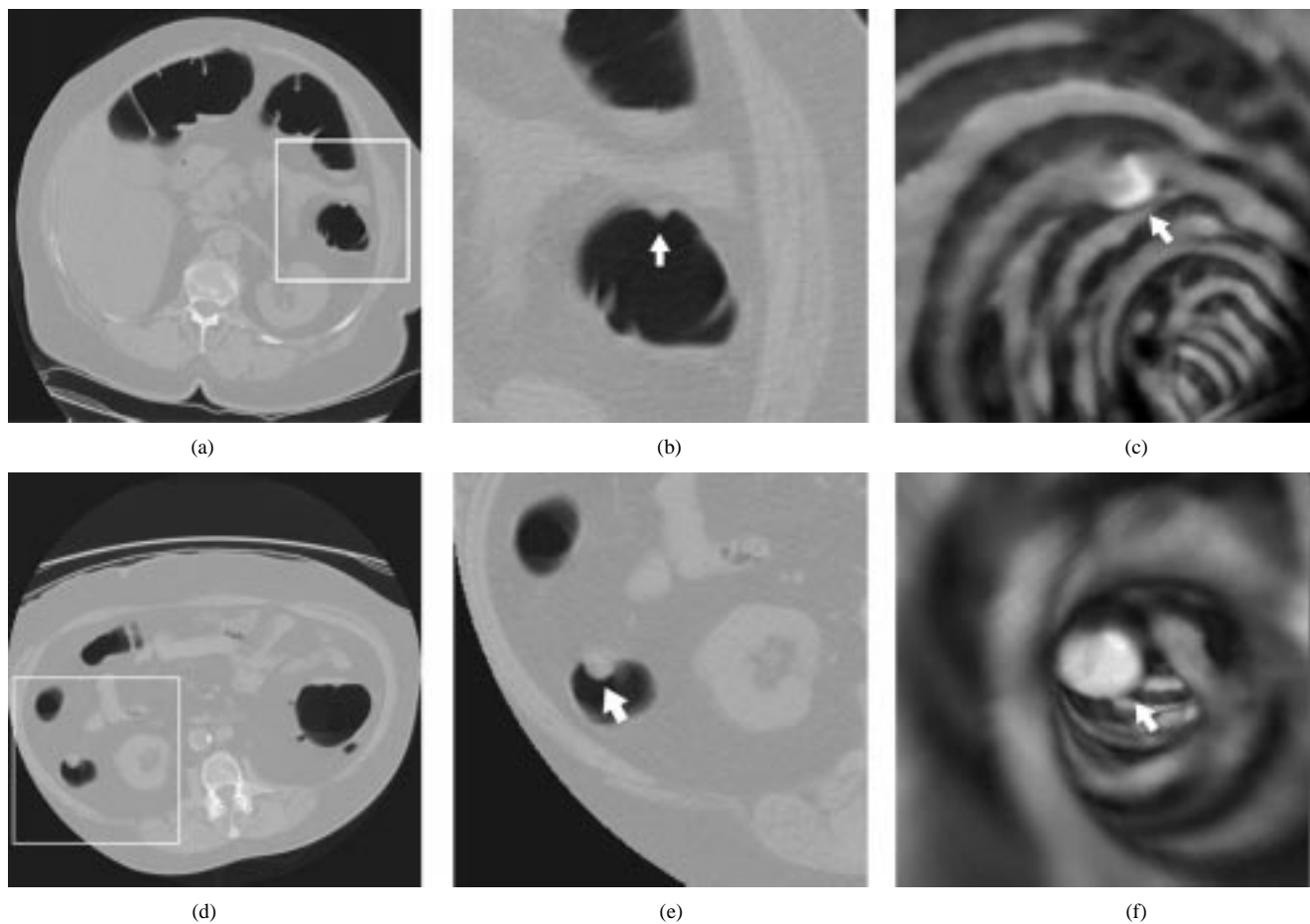


Fig. 4. Demonstration of the effect of the shape index in differentiating between polyps, folds, and lumen. (a) and (d): Axial images with polyps in the boxes. (b) and (e) Polyps are indicated by arrows. (c) and (f) Three-dimensional endoluminal views of the polyps in (b) and (e) rendered by shape index. The shape index clearly highlights the polyps (white), and differentiate them from folds (light gray) and colonic wall (dark gray).

Starting with seed regions, hysteresis thresholding based on the shape index and curvedness is applied to the extracted colon \tilde{C} to obtain polyp candidates. The hysteresis thresholding extracts a set of spatially connected voxels to the seed regions having shape index and curvedness values within the predefined minimum and maximum values that are called a *growable region*. This process is intended to extract a large connected component that corresponds to the major portion of a polyp, because the peripheral region of a polyp does not always show a perfect cap shape, but may show a dome-like shape. Therefore, we use a relaxed minimum threshold value of 0.8 for the shape index in order to include the skirts of the polyps connected to the colonic walls or folds. Similarly, the peripheral region of a polyp may have curvedness values that are smaller or larger than those of the center region of a polyp. Therefore, the minimum and maximum threshold values for curvedness are relaxed to 0.05 mm^{-1} (effective size of 20 mm) and 0.25 mm^{-1} (effective size of 4 mm), respectively, for identification of clinically significant polyps.

Table I shows the threshold values for the major parameters used in the segmentation process.

C. Clustering of Polyp Candidates

The polyp candidates may contain multiple detections, at different locations, of the same polyp, and may include a

TABLE I
THRESHOLD VALUES FOR THE MAJOR PARAMETERS USED IN THE POLYP DETECTION PROCESS

Parameter			Value
Seed region	shape index	minimum	0.9
		maximum	1.0
	curvedness	minimum	0.08 mm^{-1}
		maximum	0.20 mm^{-1}
Growable region	shape index	minimum	0.8
		maximum	1.0
	curvedness	minimum	0.05 mm^{-1}
		maximum	0.25 mm^{-1}
Merging distance			12.5 mm
Fuzzy membership			0.8
Minimum volume			38 mm^3

large number of small bumpy structures due to image noise. Multiple detections are merged into a single candidate by combining the detections that are located within a *merging distance*. We use a merging distance of approximately 10

mm, because, generally, multiple detections may occur on polyps larger than 10 mm.

Then, we employ a *fuzzy c-means algorithm* [35] to remove polyp candidates due to noise. Let $\mathbf{f}(p)$ denote the feature vector of data point p (i.e., a voxel in a polyp candidate). The fuzzy *c-means* algorithm groups the data points p with similar $\mathbf{f}(p)$ into a single cluster \mathcal{C}_i for some i . The similarity between two data points p and q is defined by the similarity measure $d(p, q) \equiv \|\mathbf{f}(p) - \mathbf{f}(q)\|$, where $\|\cdot\|$ represents the Euclidean distance. For our purpose, the main advantage of the fuzzy clustering is that it defines a membership function $\mathcal{U}_i(p) \in [0, 1]$ for each data point p and each cluster \mathcal{C}_i . If the value of $\mathcal{U}_i(p)$ is large, it is likely that p belongs to cluster \mathcal{C}_i .

To start the fuzzy clustering, we use the center of coordinates for each polyp candidate, obtained from the segmentation step in the previous section, as the initial estimate of the cluster centers. Then, for each point p , we initialize the membership function so that $\mathcal{U}_i(p) = 1$ if p belongs to the i th candidate and $\mathcal{U}_i(p) = 0$ otherwise. The feature values in each $\mathbf{f}(p)$ are normalized to the range $[0, 1]$. The fuzzy *c-means* clustering takes $\mathbf{f}(p)$ of all p as input, and moves the cluster centers to the optimal location by iteratively updating the membership functions and the location of the cluster centers. This optimization is based on minimizing an objective function J that represents the distance from any given data point to a cluster center weighted by the value of the membership function for the data point

$$J = \sum_{i=1}^{|\mathcal{C}|} \sum_p \mathcal{U}_i^2(p) d(p, c_i)$$

where c_i represents the center coordinate of cluster \mathcal{C}_i , and $|\mathcal{C}|$ is the number of polyp candidates. At each iteration, a new cluster center

$$\hat{c}_i = \frac{\sum_p p \mathcal{U}_i^2(p)}{\sum_p \mathcal{U}_i^2(p)}, \quad 1 \leq i \leq C$$

is calculated and a new membership function

$$\hat{\mathcal{U}}_i(p) = \begin{cases} 1 & \hat{c}_i = p \\ \left\{ \frac{\sum_{j=1}^C \frac{d(p, \hat{c}_i)}{d(p, \hat{c}_j)}}{\sum_{j=1}^C \frac{d(p, \hat{c}_i)}{d(p, \hat{c}_j)}} \right\}^{-1} & \hat{c}_i \neq p \end{cases}$$

is obtained for $1 \leq i \leq C$. Then $\mathcal{U}_i(p)$ is replaced with $\hat{\mathcal{U}}_i(p)$, and the iteration continues. The iteration terminates when the difference between the current and the previous values of the objective function J becomes less than a predefined threshold value.

The data points p with the value of the membership function higher than a threshold value m , $\mathcal{U}_j(p) \geq m$, for some j , are kept to yield the final clusters. By using the relatively high threshold value m of 0.8, the fuzzy clustering process keeps the candidates due to noise as a small, isolated cluster, because they tend to contain voxels that have distinctly different feature values from those of their surrounding voxels. These voxels

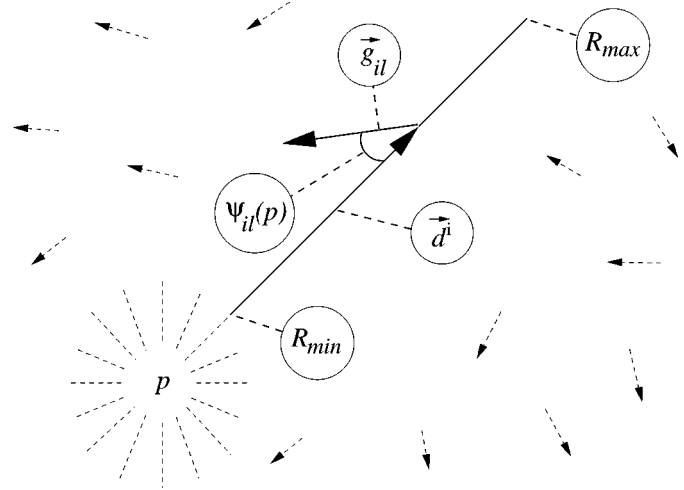


Fig. 5. The calculation of GC and DGC features at operating point p is based on considering the directions (angle $\psi_{il}(p)$) of the gradient vectors \vec{g}_{il} over a distance range $[R_{min}, R_{max}]$ in selected directions \vec{d}^i as described in the text.

have low values of the membership function for the candidates and, thus, the above thresholding operation generates small clusters. Thresholding with a minimum volume of approximately 35 mm³ is applied to individual clusters for removal of these small clusters. This minimum volume is equivalent to the volume of a 4-mm polyp, which is small enough to keep the clinically significant polyps that are 5 mm or larger.

Table I summarizes the threshold values for the major parameters used in the clustering process.

V. VOLUMETRIC FEATURES FOR REDUCING FALSE POSITIVES

Our previous polyp detection scheme [17] discriminated between polyps and FP findings by using the mean value of four features: the shape index, curvedness, CT value, and magnitude of the gradient of CT values. In the improved scheme, we introduce two new features that are based upon the concept of *gradient concentration* (GC) [36]. The application of this method for polyp detection is described in more detail in [26]. In short, the GC feature at a point p characterizes the overall direction of the gradient vectors around p . It is defined by

$$GC(p) = \frac{1}{D} \sum_{i=1}^D e_i^{\max}(p) \quad (10)$$

$$e_i^{\max}(p) = \max_{R_{min} \leq n < R_{max}} \left\{ \frac{1}{n+1} \sum_{l=0}^n \cos \psi_{il}(p) \right\} \quad (11)$$

where D is the number of the symmetrically 3-D-oriented direction vectors \vec{d}^i originating from p . The angle $\psi_{il}(p)$ is calculated between \vec{d}^i and \vec{g}_{il} , where \vec{g}_{il} is the gradient vector located at distance l from p in direction \vec{d}^i (Fig. 5).

The value of the GC feature is maximal at the center of a Gaussian sphere. However, polyps often appear to be hemispherical objects adhering to the colonic wall rather than spherical objects. Therefore, we have developed a modified GC

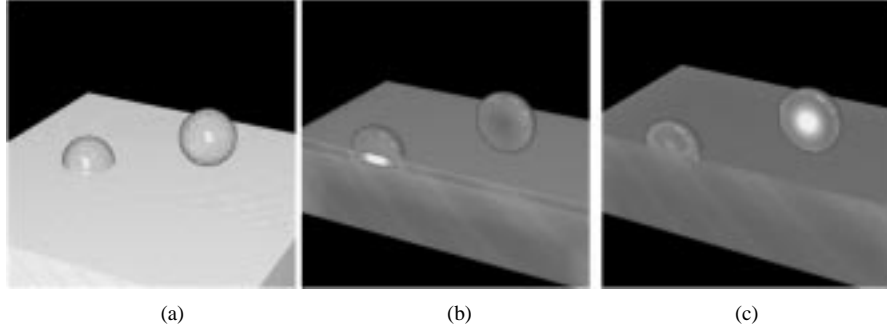


Fig. 6. (a) Phantom with a complete Gaussian sphere and a Gaussian hemisphere. (b) Cut-plane view of the gradient concentration (GC) response of the phantom shown in (a). (c) Cut-plane view of the directional gradient concentration (DGC) response of the phantom shown in (a). In (b) and (c), regions with high response are rendered white while those of low response are rendered gray.

feature, called the *directional gradient concentration* (DGC), which is computed similarly to GC, as follows:

$$DGC(p) = \frac{1}{2D} \sum_{i=1}^{D/2} \times \begin{cases} |e_i^{\max}(p) - e_{i+D/2}^{\max}(p)|; & e_i^{\max}(p), e_{i+D/2}^{\max}(p) > 0 \\ e_i^{\max}(p) + e_{i+D/2}^{\max}(p); & \text{otherwise.} \end{cases}$$

Here, e_i^{\max} and $e_{i+D/2}^{\max}$ are computed in opposite directions \vec{d}^i and $\vec{d}^{i+D/2}$. Phantom studies confirm that the DGC feature yields a higher response for hemispherical polyp-like objects than for complete spheres, whereas the opposite is true for the conventional GC feature (Fig. 6).

The six features (shape index, curvedness, CT value, gradient, GC, and DGC) were characterized by use of nine statistics. Let s_i represent a polyp candidate after fuzzy clustering, and let $f^j(p)$ represent the value of feature f^j at voxel p . Let $|s_i|$ denote the number of voxels in candidate s_i . The following nine statistics were used to characterize f^j in s_i :

$$\begin{aligned} \text{mean}(s_i, f^j) &= \mu_{ij} = \sum_{p \in s_i} \frac{f^j(p)}{|s_i|} \\ \min(s_i, f^j) &= \min_{p \in s_i} \{f^j(p)\} \\ \max(s_i, f^j) &= \max_{p \in s_i} \{f^j(p)\} \\ \text{var}(s_i, f^j) &= \sigma_{ij}^2 = \frac{1}{|s_i| - 1} \sum_{p \in s_i} (f^j(p) - \mu_{ij})^2 \\ \text{skew}(s_i, f^j) &= \frac{1}{|s_i|} \sum_{p \in s_i} \left(\frac{f^j(p) - \mu_{ij}}{\sigma_{ij}} \right)^3 \\ \text{kurt}(s_i, f^j) &= \frac{1}{|s_i|} \sum_{p \in s_i} \left(\frac{f^j(p) - \mu_{ij}}{\sigma_{ij}} \right)^4 - 3 \\ \text{entropy}(s_i, f^j) &= \sum_{p \in s_i} \text{Prob}\{p\} \ln(\text{Prob}\{p\}) \\ \text{contrast}(s_i, f^j) &= \frac{\min(s_i, f^j)}{\max(s_i, f^j)} \\ \max 10(s_i, f^j) &= \frac{1}{10} \sum_{k=1}^{10} f^j(m_k). \end{aligned}$$

In the last equation, m_k represent the voxels with the highest value(s) of f^j within s_i .

VI. DISCRIMINANT ANALYSIS

In the final stage of our CAD scheme, discriminant analysis based on 3-D volumetric feature statistics (FS) is carried out for reducing FPs among the polyp candidates. For this purpose, we employ linear discriminant analysis (LDA) and quadratic discriminant analysis (QDA) [37].

Let n denote the number of FSs used in the discriminant analysis, and let $\mathbf{F}_i = (\mathcal{F}_i^1, \mathcal{F}_i^2, \dots, \mathcal{F}_i^n)$ denote an n -dimensional (n -D) feature vector of the polyp candidate s_i , in which the component \mathcal{F}_i^j represents the j -th FS value of the polyp candidate. Given a training set with known classes, LDA or QDA generates a *decision boundary* that optimally partitions the feature space spanned by the n features into two classes, i.e., a true-positive (TP) class denoted by C_{TP} and a FP class denoted by C_{FP} . To this end, a *discriminant function* $g(\mathbf{F}_i): \mathbb{R}^n \rightarrow \mathbb{R}$ is generated, which projects the n -D feature space to a scalar *decision variable* space. The decision boundary is given by $g(\mathbf{F}_i) = 0$.

LDA uses the simplest type of discriminant function, called a linear discriminant function, defined by

$$g(\mathbf{F}_i) = \mathbf{w}^t \mathbf{F}_i + \mathbf{c} \quad (12)$$

where \mathbf{w} is an n -D weight vector, \mathbf{w}^t is the transpose of \mathbf{w} , and \mathbf{c} is a constant vector. Given a training set of candidates that are known to belong to either C_{TP} or C_{FP} , \mathbf{w} is given by

$$\mathbf{w} = (\Sigma_{TP} + \Sigma_{FP})^{-1} (\boldsymbol{\mu}_{TP} - \boldsymbol{\mu}_{FP})$$

where $(\boldsymbol{\mu}_{TP}, \Sigma_{TP})$ and $(\boldsymbol{\mu}_{FP}, \Sigma_{FP})$ are the mean feature vectors of these samples and covariance matrices of the samples in the C_{TP} and C_{FP} classes, respectively. Because of the linearity of $g(\mathbf{F}_i)$ in terms of \mathbf{F}_i , the decision boundary for LDA forms a hyperplane in the feature space. In QDA, on the other hand, g is a quadratic discriminant function defined by

$$\begin{aligned} g(\mathbf{F}_i) &= -\frac{1}{2} (\mathbf{F}_i - \boldsymbol{\mu}_{TP})^t \Sigma_{TP} (\mathbf{F}_i - \boldsymbol{\mu}_{TP}) \\ &\quad - \frac{1}{2} (\mathbf{F}_i - \boldsymbol{\mu}_{FP})^t \Sigma_{FP} (\mathbf{F}_i - \boldsymbol{\mu}_{FP}) + \mathbf{c} \end{aligned}$$

and, thus, the decision boundary forms a hyperquadratic surface. In the following, we will denote both types of discriminant functions simply by $g(\mathbf{F}_i)$.

Geometrically, the discriminant function $g(\mathbf{F}_i)$ is interpreted as proportional to the signed distance from \mathbf{F}_i to the decision boundary. Generally, the larger the value of $g(\mathbf{F}_i)$, the more likely it is that s_i is a polyp. In other words, $g(\mathbf{F}_i)$ is proportional to the ranked ordering of the likelihood that s_i is a polyp. Therefore, we classify the polyp candidates into classes C_{TP} and C_{FP} by partitioning the feature space through thresholding of the decision variable as follows:

$$\begin{aligned} C_{TP} &= \{\mathbf{F}_i; g(\mathbf{F}_i) \geq t\} \\ C_{FP} &= \{\mathbf{F}_i; g(\mathbf{F}_i) < t\}. \end{aligned} \quad (13)$$

Those candidates that are classified in the polyp class C_{TP} are reported as the final detected polyps by the CAD scheme.

VII. PERFORMANCE EVALUATION

A. Database of Polyps in CTC

To evaluate the performance of our CAD scheme, we collected 43 CTC cases retrospectively at the University of Chicago Hospitals. These cases were obtained by use of a helical CT scanner (GE CTi 9800, General Electric Medical Systems, Milwaukee WI) with collimation of 5 mm, a pitch of 1.5–1.7, and reconstruction intervals of 1.5–2.5 mm. The current was 100 mA with 120 kVp. A 180° linear interpolation and the standard reconstruction algorithm were used. The colon was cleansed with a standard precolonoscopy cleansing method and insufflated with room air when the CT scanning was performed. Each patient was scanned in both supine and prone positions.

Eleven of the cases contained a total of 12 colonoscopy-proven polyps of at least 5 mm in diameter. This size is the lower limit of the size range for the polyps that are considered to be clinically significant [3]. Nine polyps measured between 5 and 10 mm; the other three measured 12, 25, and 30 mm. Two experienced radiologists examined the locations of these polyps in the CTC data sets. As a result, all of the polyps were confirmed on the CT images, but three polyps were visible only in either the supine or prone view, because they were located in a collapsed region or buried under the fluid in the other view. Therefore, we had a total of 21 visible polyps. Because two of these visible polyps were in a single data set, we had 20 CTC data sets, among 86 data sets, with at least one visible polyp.

Each CTC data set covered the entire region of the abdomen, from diaphragm to rectum, and consisted of 150–300 CT images with a matrix size of 512×512 . After the linear interpolation along the axial direction, the z dimension of the resulting isotropic volumes contained between 500 and 700 voxels, and the physical resolution of these volumes was 0.5–0.75 mm/voxel.

B. Evaluation of the Detection of Polyp Candidates

To determine the TPs and FPs in the computerized detections, we determined the center coordinates of the TP polyps in each data set by the two radiologists. A CAD detection was considered a TP if the distance between the detected polyp and the center of a true polyp was at most 15 mm. All other findings were considered FPs.

C. Evaluation of Discriminant Analysis

We evaluated the performance of the LDA and QDA in differentiating polyps from FPs by regarding the output of the discriminant function as a decision variable, and subjecting the values of the discriminant function $g(\mathbf{F}_i)$ for each candidate s_i to receiver operating characteristic (ROC) analysis [38]. To estimate the unbiased performance, we trained and tested the classifiers for LDA and QDA by a *round-robin* (or *leave-one-out*) method [39]. In this method, each candidate s_i is removed, in turn, from the set of all polyp candidates $\Omega = \{s_i\}_{1 \leq i \leq K}$. Here, K represents the number of polyp candidates after the fuzzy clustering. The classifier is trained by the remaining candidates $\Omega \setminus \{s_i\}$, and a discriminant function $g(\mathbf{F}_i)$ is generated and evaluated on the removed candidate s_i . The set $\{g(\mathbf{F}_i)\}_{1 \leq i \leq K}$ is subjected to the LABROC4 program [40], and the area under the ROC curve (A_z) is calculated. Generally, a larger A_z value indicates a higher performance in the discrimination task. The advantage of this method is that the training and testing of candidates can be completely separated; therefore, the resulting discrimination criterion is least biased to the cases in the database. Another advantage is that almost all of the polyp candidates are available in this method.

D. Evaluation of Overall Performance

We obtained the final detected polyps by determining the threshold value t in (13). Correspondingly, we generated a free-response ROC (FROC) curve that indicates the overall performance by using t as the sweeping variable. For this purpose, we first generated the discriminant function $g(\mathbf{F}_i)$ by use of the entire set of polyp candidates $\{s_i\}_{1 \leq i \leq K}$. Then FROC curves were generated by the following two methods: 1) a FROC curve based on cases (patients) and 2) a FROC curve based on the volumetric data sets. In both methods, the CAD scheme processed independently the supine and prone volumetric data sets generated from a single patient to yield polyp candidates. In 1), a case with polyps was regarded as being correctly recognized as abnormal if a polyp in the case was detected in either the supine or the prone data set in the case. In 2), supine and prone data sets in a case were considered as different data sets, and each data set was considered to be correctly recognized as abnormal if a polyp observed in the data set was detected.

VIII. RESULTS

A. Performance of the Detection of Polyp Candidates

Table I summarizes the major parameter settings that were used in the polyp segmentation process (Section IV-B) and the clustering process (Section IV-C). As a result of the polyp segmentation process, all visible polyps were detected, except for one polyp in the supine view of a patient. However, this missed polyp was detected in the prone view of the same patient. Therefore, all the polyps were detected in either the supine or prone data set of a patient. The detection process produced 3162 FPs, yielding approximately 37 FPs/data set, or 74 FPs/case. This number was reduced after the clustering process, which yielded 1096 FPs, i.e., approximately 13 FPs/data set, or 26 FPs/case.

TABLE II
SELECTED RESULTS OF ROC ANALYSIS. A_z VALUES FOR SELECTED
COMBINATIONS OF FEATURE STATISTICS

Feature-statistic combination	$A_z(L)$	$A_z(Q)$
$\mu_{SI}, \mu_{DGC}, \nu_{CT}$	0.95	0.95
$\mu_{SI}, \mu_{CT}, \mu_{GR}$	0.94	0.95
μ_{SI}, ν_{CT}	0.94	0.93
$\mu_{SI}, \mu_{DGC}, \nu_{CV}$	0.93	0.95
$\mu_{SI}, \mu_{CT}, \mu_{GR}, \mu_{CV}$	0.92	0.93

Selected results of ROC analysis. A_z values for selected combinations of feature statistics are shown below. $A_z(L)$ and $A_z(Q)$ indicate the A_z values obtained by LDA and QDA with round-robin test, respectively. Here, μ and ν represent the mean and variance statistics, respectively. The acronyms for the features are: CT = CT value, GR = gradient magnitude, SI = shape index, CV = curvedness, DGC = directional gradient concentration. For example, μ_{SI} indicates the mean of shape index values whereas ν_{CT} indicates the variance of ct values.

B. Performance of Discriminant Analysis

Table II shows the results of the round-robin test for several FS combinations. Among various combinations of the FSs, this table lists only those combinations that show a high performance in discriminating polyps from FPs. The A_z values obtained by LDA and QDA are shown in the first ($A_z(L)$) and the second ($A_z(Q)$) columns, respectively. The last row shows the FS combination used in our CAD scheme reported previously [17]. As demonstrated in the other rows, use of a new feature such as the mean of the DGC, and the new statistics of the previous features such as the variance of CT values, are shown to increase the A_z values of both LDA and QDA.

C. Overall Performance

To evaluate the overall performance of our CAD scheme, we generated FROC curves in the manner described in Section VII-D. Among several combinations of FSs, the best result was obtained by applying the QDA to the feature space spanned by the FSs in the first row of Table II. The decision boundary generated by QDA is shown by a black curve in Fig. 7(a)–(c). As shown in this figure, the decision boundary separates TPs (black squares) from FPs (gray dots) well. Two FROC curves were generated [Fig. 7(d)]. The FROC curve showing the performance based on data sets is represented by a dotted curve, whereas that based on cases is represented by a solid curve. These FROC curves indicate that the CAD scheme yielded 95% sensitivity with 1.2 FPs/data set, or 100% sensitivity with 2.0 FPs/case.

IX. DISCUSSION

In this paper, we have presented a CAD scheme for the detection of polyps in CTC. The high sensitivity and low FP rate in our preliminary results show the promise of computerized detection methods as a potential aid for interpreting CTC examinations.

In Section II, we described a process of generating an isotropic volume that is used in the 3-D processing in the subsequent steps. This process also serves to eliminate the differences in the CT parameter settings—in particular, the reconstruction intervals—among different data sets. In our study, no significant visual difference, or difference in detection

results, was observed. It should be noted that we used CT parameter settings that are currently used as a standard protocol for the CTC examinations [3]. This protocol is widely accepted because it allows one to acquire CTC images in which the visibility and conspicuity of clinically significant sizes of polyps are high regardless of the CT scanner used for the acquisition process [41]. However, the visibility and conspicuity of polyps may depend largely on the image acquisition parameters [16], [42]; thus, our CAD scheme may yield a different performance if a nonstandard CT parameter setting is used. Further work is needed for clarifying the dependence of the performance of the CAD scheme on CTC parameter settings and for developing an optimization method of the CAD scheme, such as the one described in [43], for different parameter settings.

Reliable automated segmentation of the colonic walls is a necessary first step for successful automated polyp detection. Our knowledge-guided technique presented in Section III segments the colonic walls at a thickness of 3–4 mm and excludes most or all of the extra-colonic components from the segmented colon. These characteristics of the technique yield a high sensitivity and low FP rate in the detection of polyps. However, an evaluation of our colon segmentation method indicates that the FP rate could still be reduced by approximately 10% if all of the extra-colonic components remaining after the knowledge-guided colon segmentation could be removed [26].

Our detection method based on the shape index (Section IV) assumes that polyps appear as a cap-like shape, i.e., as polypoid lesions. Recently, clinical researchers are investigating flat lesions that may have an incidence ranging between 8% and 30%, and may have significantly different biologic features than polypoid lesions [44], [45]. These flat lesions have the potential to transform to high-grade dysplasia quickly, and to invade the submucosa rapidly. They tend to be smaller than the typical polypoid adenomas and therefore can be difficult to detect by conventional colonoscopy. Radiologists have found that detecting flat regions is more difficult in CTC than in colonoscopy [46]. Because of the difficulty in finding the flat lesions in CTC and the uncertainty of their clinical importance, we did not specifically design our method to detect these lesions and, thus, our CAD may not be able to detect them effectively. Detection of flat lesions remains for future investigation when clinical studies confirm the importance of the detection of these lesions for screening of colon cancers.

At the beginning of the clustering process, polyp candidates within a predefined distance are merged to generate a single detection from a polyp. However, we observed that multiple detections may still occur from polyps larger than 20 mm. In this study, the detection closest to the true polyp location was used as the detected polyp, and the others were considered as FPs. Simply relaxing the tolerance distance may merge a large number of FPs to TPs and, thus, may produce incorrect results in terms of sensitivity. This indicates that an additional method needs to be developed for reliable detection of a large polyp. The current hysteresis thresholding scheme for segmenting polyps is based on shape index and curvedness features alone. Therefore, a part of the local region that is more appropriate in identifying polyps with the other features could be excluded, which may increase the FP rate. It is, thus, necessary to investigate whether

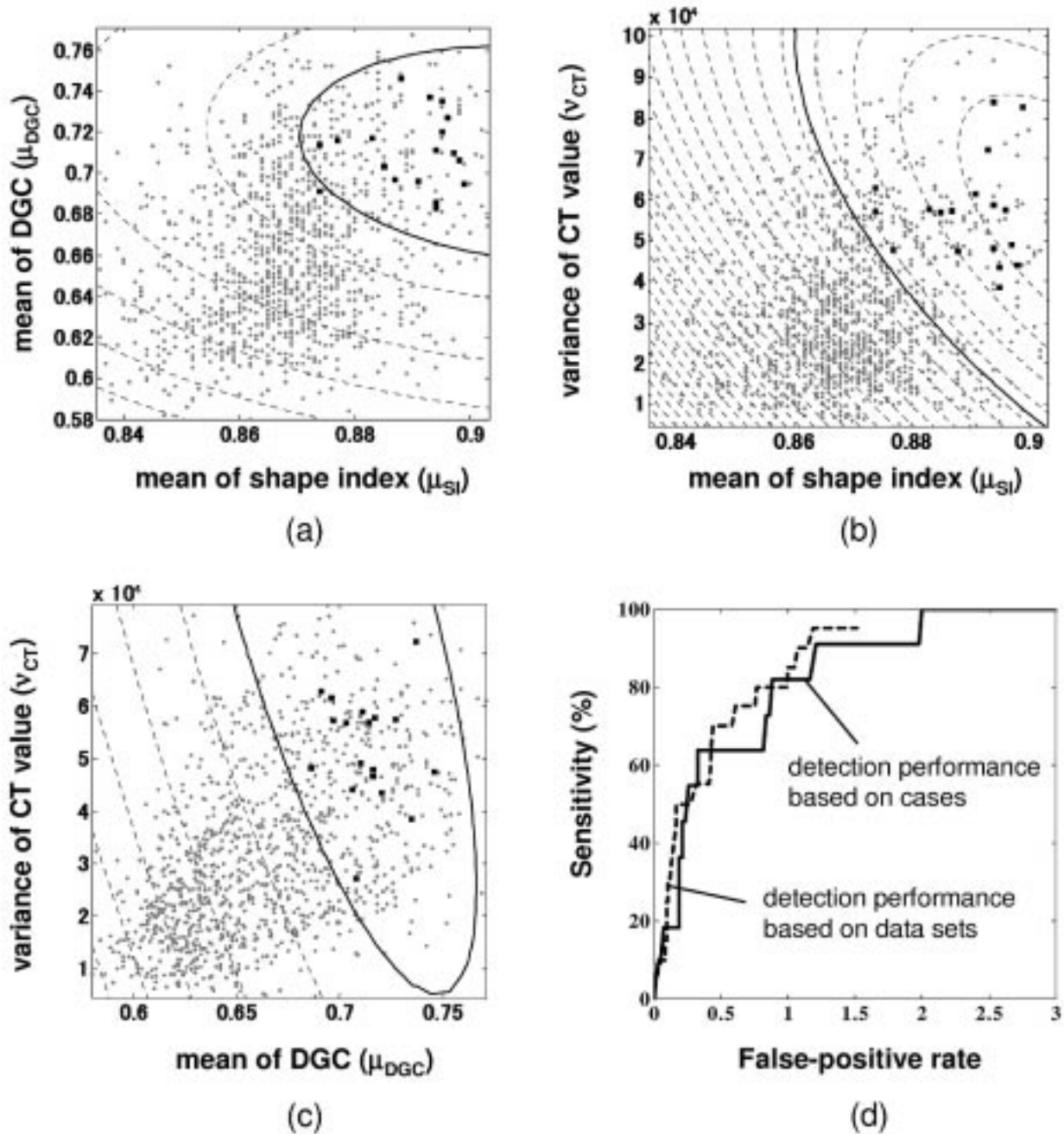


Fig. 7. (a)–(c) Distributions of the values of the three feature statistics for the polyp candidates obtained by our CAD scheme. TPs are represented by black square boxes and FPs are represented by gray dots. Decision boundaries generated by QDA are shown by solid curves. Dotted curves show the iso-surfaces of the discrimination function generated by QDA. (d) FROC curves generated from the result of QDA shown in (a)–(c). The solid curve represents the detection performance of the CAD scheme based on cases, whereas the dotted curve shows the performance based on data sets.

the polyp segmentation scheme needs to be modified to include optimal regions for each feature.

Other classifiers, such as neural networks, could be used to improve the FP rate of the polyp discrimination. However, proper use of neural networks requires large independent and representative sets of training and testing data. The size of our polyp database should therefore be increased before such an analysis is attempted.

The current implementation of the CAD scheme has not been optimized for speed and efficiency. Using a PC workstation (Marquis K120-SR, ASL Inc., Newark CA) with dual proces-

sors (Athlon MP 1.2 GHz, AMD, Sunnyvale CA), the whole process of detecting polyps in a data set takes approximately 10 min depending on the size of the volume.

We used only a small number of polyps in the evaluation of the overall performance of our CAD scheme and, thus, we are limited in making generalizations about the detection accuracy of our scheme. The FROC curves were generated by a consistency test. No evaluation based on an independent database was performed. As indicated in Fig. 7(a)–(c), the TPs were quite concentrated in a small region in the feature space, which indicates that the feature statistics characterize the true polyps well.

Although our method appears promising, extension to a larger database will be needed for confirmation of the usefulness of the CAD scheme for screening.

X. CONCLUSION

We have developed an improved CAD scheme for the detection of polyps in CTC. Based on clinical CTC cases, our CAD scheme yielded a high performance of 100% sensitivity with 2.0 FPs/patient. If this result can be translated into a larger number of cases, radiologists will need to interpret only a few regions indicated by the CAD scheme in a CTC examination. Such a "second opinion" offered by a CAD scheme will substantially reduce radiologists' interpretation time and improve their performance in the detection of colonic polyps in CTC. Therefore, our CAD scheme has the potential of making CTC a viable option for screening of large patient populations, resulting in early detection of colon cancers, and leading to reduced mortality due to colon cancer.

ACKNOWLEDGMENT

The authors would like to thank Dr. A. H. Dachman, Dr. P. MacEaney, and Dr. D. Rubin, for providing the authors with CTC cases. They would also like to thank the members of the Kurt Rossmann Laboratories in the Department of Radiology at The University of Chicago for helpful discussions and E. Lanzl for improving the manuscript.

REFERENCES

- [1] M. J. O'Brien, S. J. Winawer, A. G. Zauber, L. S. Gottlieb, S. S. Sternberg, B. Diaz, G. R. Dickersin, S. Ewing, S. Geller, and D. Kasimian *et al.*, "The national polyp study: Patient and polyp characteristics associated with high-grade dysplasia in colorectal adenomas," *Gastroenterology*, vol. 98, pp. 371–379, 1990.
- [2] S. J. Winawer, R. H. Fletcher, L. Miller, F. Godlee, M. H. Stolar, C. D. Mulrow, S. H. Woolf, S. N. Glick, T. G. Ganiats, J. H. Bond, L. Rosen, J. G. Zapka, S. J. Olsen, F. M. Giardiello, J. E. Sisk, R. Van Antwerp, C. Brown-Davis, D. A. Marciniak, and R. J. Mayer, "Colorectal cancer screening: Clinical guidelines and rationale," *Gastroenterology*, vol. 112, pp. 594–642, 1997.
- [3] C. D. Johnson and A. H. Dachman, "CT colonography: The next colon screening examination?," *Radiology*, vol. 216, pp. 331–341, 2000.
- [4] D. J. Vining, "Virtual colonoscopy," *Gastrointest. Endosc. Clin. N. Amer.*, vol. 7, pp. 285–291, 1997.
- [5] ———, "Virtual colonoscopy," *Semin. Ultrasound CT MR*, vol. 20, pp. 56–60, 1999.
- [6] A. H. Dachman, J. K. Kuniyoshi, C. M. Boyle, Y. Samara, K. R. Hoffmann, D. T. Rubin, and I. Hanan, "CT colonography with three-dimensional problem solving for detection of colonic polyps," *Amer. J. Roentgenol.*, vol. 171, pp. 989–995, 1998.
- [7] G. D. Rubin, C. F. Beaulieu, V. Argiro, H. Ringl, A. M. Norbash, J. F. Feller, M. D. Dake, R. B. Jeffrey, and S. Napel, "Perspective volume rendering of CT and MR images: Applications for endoscopic imaging," *Radiology*, vol. 199, pp. 321–330, 1996.
- [8] A. P. Royster, H. M. Fenlon, P. D. Clarke, D. P. Nunes, and J. T. Ferrucci, "CT colonoscopy of colorectal neoplasms: Two-dimensional and three-dimensional virtual-reality techniques with colonoscopic correlation," *Amer. J. Roentgenol.*, vol. 169, pp. 1237–1242, 1997.
- [9] J. G. Fletcher, C. D. Johnson, R. L. MacCarty, T. J. Welch, J. E. Reed, and A. K. Hara, "CT colonography: Potential pitfalls and problem-solving techniques," *Amer. J. Roentgenol.*, vol. 172, pp. 1271–1278, 1999.
- [10] J. G. Fletcher, C. D. Johnson, T. J. Welch, R. L. MacCarty, D. A. Ahlquist, J. E. Reed, W. S. Harmsen, and L. A. Wilson, "Optimization of CT colonography technique: Prospective trial in 180 patients," *Radiology*, vol. 216, pp. 704–711, 2000.
- [11] H. M. Fenlon, D. P. Nunes, P. C. Schroy, III, M. A. Barish, P. D. Clarke, and J. T. Ferrucci, "A comparison of virtual and conventional colonoscopy for the detection of colorectal polyps," *N. Eng. J. Med.*, vol. 341, pp. 1496–1503, 1999.
- [12] P. Pescatore, T. Glucker, J. Delarive, R. Meuli, D. Pantoflickova, B. Duvoisin, P. Schnyder, A. L. Blum, and G. Dorta, "Diagnostic accuracy and interobserver agreement of CT colonography (virtual colonoscopy)," *Gut*, vol. 47, pp. 126–130, 2000.
- [13] D. K. Rex, D. Vining, and K. K. Kopecky, "An initial experience with screening for colon polyps using spiral CT with and without CT colonography (virtual colonoscopy)," *Gastrointest. Endosc.*, vol. 50, pp. 309–313, 1999.
- [14] D. Rex, Lecture, presented at the at Digestive Disease Week, 2000.
- [15] A. H. Dachman, J. Lieberman, R. B. Osnis, S. Y. Chen, K. R. Hoffmann, C. T. Chen, G. M. Newmark, and J. McGill, "Small simulated polyps in pig colon: Sensitivity of CT virtual colonography," *Radiology*, vol. 203, pp. 427–430, 1997.
- [16] C. F. Beaulieu, S. Napel, B. L. Daniel, I. Y. Chén, G. D. Rubin, I. M. Johnstone, and R. B. Jeffrey, Jr, "Detection of colonic polyps in a phantom model: Implications for virtual colonoscopy data acquisition," *J. Comput. Assist. Tomogr.*, vol. 22, pp. 656–663, 1998.
- [17] H. Yoshida, Y. Masutani, P. MacEaney, D. Rubin, and A. H. Dachman, "Computerized detection of colonic polyps in CT colonography based on volumetric features: A pilot study," *Radiology*, 2002.
- [18] R. M. Summers, C. F. Beaulieu, L. M. Pusanik, J. D. Malley, R. B. Jeffrey, Jr, D. I. Glazer, and S. Napel, "Automated polyp detector for CT colonography: Feasibility study," *Radiology*, vol. 216, pp. 284–290, 2000.
- [19] R. M. Summers, C. D. Johnson, L. M. Pusanik, J. D. Malley, A. M. Youssef, and J. E. Reed, "Automated polyp detection at CT colonography: Feasibility assessment in a human population," *Radiology*, vol. 219, pp. 51–59, 2001.
- [20] D. J. Vining, G. W. Hunt, D. K. Ahn, D. R. Stelts, and P. F. Hemler, "Computer-assisted detection of colon polyps and masses," *Radiology*, vol. 205(P), p. 705, 1997.
- [21] D. J. Vining, Y. Ge, D. K. Ahn, and D. R. Stelts *et al.*, "Virtual colonoscopy with computer-assisted polyp detection," in *Computer-Aided Diagnosis in Medical Imaging*, K. Doi *et al.*, Eds. Amsterdam, The Netherlands: Elsevier Science, 1999, pp. 445–452.
- [22] D. S. Paik, C. F. Beaulieu, R. B. Jeffrey, C. Karadi, and S. Napel, "Detection of polyps in CT colonography: A comparison of a computer-aided detection algorithm to 3D visualization methods," *Radiology*, vol. 213(P), p. 193, 1999.
- [23] D. S. Paik, C. F. Beaulieu, R. B. Jeffrey, J. Yee, A. M. Steinauer-Gebauer, and S. Napel, "Computer aided detection of polyps in CT colonography: Method and free-response ROC evaluation of performance," *Radiology*, vol. 217(P), p. 370, 2000.
- [24] D. Chen, Z. Liang, M. R. Wax, L. Li, B. Li, and A. E. Kaufman, "A novel approach to extract colon lumen from CT images for virtual colonoscopy," *IEEE Trans. Med. Imag.*, vol. 19, pp. 1220–1226, Dec. 2000.
- [25] Y. Masutani, H. Yoshida, P. MacEaney, and A. H. Dachman, "Automated segmentation of colonic walls for computerized detection of polyps in CT colonography," *J. Comput. Assist. Tomogr.*, vol. 25, pp. 629–638, 2001.
- [26] J. Näppi, P. MacEaney, A. Dachman, and H. Yoshida, "Knowledge-guided automated segmentation of colon for computer-aided detection of polyps in CT colonography," *J. Comput. Assist. Tomogr.*, 2002, to be published.
- [27] J. J. Koenderink, *Solid Shape*. Cambridge, Massachusetts: MIT Press, 1990.
- [28] C. Dorai and A. K. Jain, "COSMOS—A representation scheme for 3D free-form objects," *IEEE Trans. Pattern Anal. Machine Intell.*, vol. 19, pp. 1115–1130, Oct. 1997.
- [29] Y. Kawata, N. Niki, H. Ohmatsu, R. Kakinuma, K. Eguchi, M. Kaenko, and N. Moriyama, "Quantitative surface characterization of pulmonary nodules based on thin-section CT images," *IEEE Trans. Nucl. Sci.*, vol. 45, pp. 2132–2138, Aug. 1998.
- [30] S. Kobayashi and K. Nomizu, *Foundations of Differential Geometry*. New York: Interscience, 1963, vol. 1.
- [31] J.-P. Thirion and A. Gourdon, "Computing the differential characteristics of isointensity surfaces," *Soumis à Computer Vision Graphics and Image Processing*, 1992.

- [32] O. Monga and S. Benayoun, "Using partial derivatives of 3D images to extract typical surface features," *Soumis à Computer Vision Graphics and Image Processing*, 1992.
- [33] O. Faugeras, *Three-Dimensional Computer Vision: A Geometric Viewpoint*. Cambridge, MA: MIT Press, 1993.
- [34] G. Lohmann, *Volumetric Image Analysis*. New York: Wiley, 1998.
- [35] A. Jain, P. Duin, and J. Mao, "Statistical pattern recognition: A review," *IEEE Trans. Pattern Anal. Machine Intell.*, vol. 22, pp. 4–37, Jan. 2000.
- [36] H. Kobatake and M. Murakami, "Adaptive filter to detect rounded convex regions: Iris filter," in *Proc. Int. Conf. Pattern Recognition*, vol. II, 1996, pp. 340–344.
- [37] K. Fukunaga, *Introduction to Statistical Pattern Recognition*. San Diego: Academic Press, 1990.
- [38] C. E. Metz, "Some practical issues of experimental design and data analysis in radiological ROC studies," *Investigat. Radiol.*, vol. 24, pp. 234–245, 1989.
- [39] E. Efron, *The Jackknife, the Bootstrap, and Other Resampling Plans*, PA: Soc. Ind. Appl. Math., 1982.
- [40] C. E. Metz, B. Herman, and J. H. Shen, "Maximum likelihood estimation of receiver operating characteristic (ROC) curves from continuously-distributed data," *Statist. Med.*, vol. 17, pp. 1033–1053, 1998.
- [41] A. K. Hara, C. D. Johnson, R. L. MacCarty, T. J. Welch, C. H. McColough, and W. S. Harmsen, "CT colonography: Single- versus multi-detector row imaging," *Radiology*, vol. 219, pp. 461–465, 2001.
- [42] E. G. McFarland, J. A. Brink, T. K. Pilgram, J. P. Heiken, D. M. Balfe, D. A. Hirsch, L. Weinstock, and B. Littenberg, "Spiral CT colonography: Reader agreement and diagnostic performance with two- and three-dimensional image-display techniques," *Radiology*, vol. 218, pp. 375–383, 2001.
- [43] M. A. Anastasio, H. Yoshida, R. Nagel, R. M. Nishikawa, and K. Doi, "A genetic algorithm-based method for optimizing the performance of a computer-aided diagnosis scheme for detection of clustered microcalcifications in mammograms," *Med. Phys.*, vol. 25, pp. 1613–1620, 1998.
- [44] Y. Saitoh, I. Waxman, A. B. West, N. K. Popnikolov, Z. Gatalica, J. Watari, T. Obara, Y. Kohgo, and P. J. Pasricha, "Prevalence and distinctive biologic features of flat colorectal adenomas in a North American population," *Gastroenterology*, vol. 120, pp. 1657–1665, 2001.
- [45] B. J. Rembacken, T. Fujii, A. Cairns, M. F. Dixon, S. Yoshida, D. M. Chalmers, and A. T. Axon, "Flat and depressed colonic neoplasms: A prospective study of 1000 colonoscopies in the UK," *Lancet*, vol. 355, pp. 1211–1214, 2000.
- [46] A. K. Hara, C. D. Johnson, and J. E. Reed, "Colorectal lesions: Evaluation with CT colography (discussion)," *Radiographics*, vol. 17, pp. 1157–1167, 1997.